



# Characterization of Planar Defect in Layered Perovskite Photocatalyst Y<sub>2</sub>Ti<sub>2</sub>O<sub>5</sub>S<sub>2</sub> by Electron Microscopy and First-Principles Calculations

Nakabayashi, Mamiko ; Nishiguchi, Kazutaka ; Liang, Xizhuang ; Hisatomi, Takashi ; Takata, Tsuyoshi ; Tsuchimochi, Takashi ; Shibata, ...

## (Citation)

The Journal of Physical Chemistry C, 127(16):7887-7893

## (Issue Date)

2023-04-27

## (Resource Type)

journal article

## (Version)

Accepted Manuscript

## (Rights)

This document is the Accepted Manuscript version of a Published Work that appeared in final form in The Journal of Physical Chemistry C, copyright © American Chemical Society after peer review and technical editing by the publisher. To access the final edited and published work see <https://doi.org/10.1021/acs.jpcc.3c00820>

## (URL)

<https://hdl.handle.net/20.500.14094/0100485303>



# Characterization of Planar Defect in Layered Perovskite Photocatalyst $\text{Y}_2\text{Ti}_2\text{O}_5\text{S}_2$ by Electron Microscopy and First-Principles Calculations

Mamiko Nakabayashi,<sup>†,@</sup> Kazutaka Nishiguchi,<sup>‡,@</sup> Xizhuang Liang,<sup>¶</sup> Takashi Hisatomi,<sup>§</sup> Tsuyoshi Takata,<sup>§</sup> Takashi Tsuchimochi,<sup>‡,||</sup> Naoya Shibata,<sup>†,⊥</sup> Kazunari Domen,<sup>\*,§,#</sup> and Seiichiro L. Ten-no<sup>\*,‡</sup>

<sup>†</sup>*Institute of Engineering Innovation, School of Engineering, The University of Tokyo, 2-11-16, Yayoi, Bunkyo-ku, Tokyo 113-8656, Japan*

<sup>‡</sup>*Graduate School of System Informatics, Kobe University, 1-1 Rokkodai-Cho, Nada-Ku, Kobe, 657-8501, Japan*

<sup>¶</sup>*School of Environmental and Material Engineering, Yantai University, 30 Qingquan Road, Yantai, 264005, China*

<sup>§</sup>*Research Initiative for Supra-Materials, Interdisciplinary Cluster for Cutting Edge Research, Shinshu University, 4-17-1 Wakasato, Nagano-city, Nagano 380-8553, Japan*

<sup>||</sup>*PRESTO, Japan Science and Technology Agency (JST), 4-1-8 Honcho Kawaguchi, Saitama, 332-0012, Japan*

<sup>⊥</sup>*Nanostructures Research Laboratory, Japan Fine Ceramic Center, Japan*

<sup>#</sup>*Office of University Professors, The University of Tokyo, 2-11-16, Yayoi, Bunkyo-ku, Tokyo 113-8656, Japan*

<sup>@</sup>Contributed equally to this work

E-mail: domen@chemsys.t.u-tokyo.ac.jp; tenno@garnet.kobe-u.ac.jp

## Abstract

Layered perovskite  $\text{Y}_2\text{Ti}_2\text{O}_5\text{S}_2$  is a promising semiconductor photocatalyst with an electronic structure suitable for overall water splitting under visible light. However, similar to other photocatalysts, structural defects during synthesis should be controlled. Transmission electron microscopy (TEM) revealed extremely large planar defects composed of S-Mg-S layers in  $\text{Y}_2\text{Ti}_2\text{O}_5\text{S}_2$  synthesized using the flux method. We determined the planar defect structure and electronic structure using first-principles calculations based on the density functional theory. The evaluation of the formation energy suggests that S- and Mg-poor conditions may prevent defect formation. Furthermore, we discuss the impurity levels caused by the planar defects and their effects on the electronic state and catalytic performance.

## Introduction

“Green Hydrogen” is now attracting worldwide attention as a clean energy source. In particular, “solar hydrogen production”, which produces green hydrogen at a lower cost using only sunlight, water, and catalysts, is promising.<sup>1-4</sup> Highly efficient water splitting photocatalysts are the key to this solar hydrogen production. Photocatalysts should generally be able to split water under visible light ( $400\text{ nm} \leq \lambda \leq 800\text{ nm}$ ) for effective utilization of solar energy because the intensity of sunlight has a peak in this wavelength region.

Previously, most photocatalysts active in the overall water splitting reaction were based on oxides with band gap energies larger than 3 eV and did not respond to visible light. However,  $\text{Y}_2\text{Ti}_2\text{O}_5\text{S}_2$  (YTOS), an oxysulfide photocatalyst, was recently proven to be active in the overall water splitting reaction under visible light with wavelengths of up to 640 nm.<sup>5</sup> The co-loading of hydrogen evolution and oxygen evolution cocatalysts, as well as fine adjustment of the pH of the reaction solution are crucial for achieving steady water splitting. However, YTOS was synthesized using a solid-state reaction method with particle sizes exceeding 10  $\mu\text{m}$ . This is extremely large for photocatalytic applications when compared to the typical particle size of photocatalysts, which is less than 1  $\mu\text{m}$ . YTOS with smaller particle sizes can be synthesized by  $\text{H}_2$  S sulfurization;<sup>6</sup>

however, the Ti species in YTOS are readily reduced because of the reductive atmosphere of  $\text{H}_2\text{S}$ , and the resultant YTOS is not highly active. Therefore, a technique for synthesizing YTOS with both a small particle size and high semiconductor quality must be developed.

The flux method, a liquid-phase process, is effective in improving the crystallinity and controlling the morphology of semiconductor photocatalysts. The most active Al-doped  $\text{SrTiO}_3$  photocatalyst, capable of splitting water into hydrogen and oxygen at quantum efficiencies close to unity, was produced using the flux method.<sup>4</sup> Moreover, oxysulfide photocatalysts have been synthesized using the flux method.  $\text{Sm}_2\text{Ti}_2\text{O}_5\text{S}_2$ , a layered perovskite-type oxysulfide synthesized by the flux method, is composed of thin plate-like particles that reflect the crystal structure and exhibits improved photocatalytic activity.<sup>7,8</sup> We attempted to synthesize YTOS using flux methods, influenced by these early studies. However, in our preliminary investigations, the resulting YTOS contained impurities and exhibited characteristic structural defects. Furthermore, contamination of the product with impurities from flux reagents is a disadvantage of the flux method, which can be particularly problematic when semiconductor materials are used as photocatalysts. Therefore, it is important to understand the structure and formation mechanism of defects in YTOS synthesized using the flux method.

(Scanning) transmission electron microscopy ((S)TEM) is a powerful tool for the direct observation of local structures inside particles. Combining these techniques with energy-dispersive X-ray spectroscopy (EDS) and electron energy loss spectroscopy (EELS) allows for the acquisition of information about the composition and chemical states with high spatial resolution. For example, in a recent study on a highly active Al-doped  $\text{SrTiO}_3$  photocatalyst, electron microscopy revealed facet-selective deposition of hydrogen and oxygen evolution cocatalysts.<sup>4</sup> Because of the mixing of reduction and oxidation sites, this is one of the key factors in suppressing unwanted charge recombination. In addition, theoretical calculations are becoming powerful tools for understanding the mechanisms of catalytic properties. First-principles approaches have successfully addressed the characteristic structures of defects and surfaces such as those of photocatalysts of multiple oxides for  $\text{H}_2\text{O}_2$  evolution.<sup>9</sup>



The internal structure and crystallinity of the oxysulfide semiconductor photocatalyst, YTOS, were analyzed using TEM and STEM-EDS in this study. First-principles calculations based on the density functional theory were performed, and the structures of the defects and their electronic states were analyzed. Subsequently, we discuss the impurity levels caused by the defects and their effects on the electronic states and catalytic performance.

## Experimental section

### Preparation of YTOS flux sample

The YTOS powder was prepared using a flux-assisted method.  $\text{Y}_2\text{S}_3$  (99.9 %, High Purity Chemical Laboratory Co., Ltd.),  $\text{Y}_2\text{O}_3$  (99.99 %, FUJIFLM Wako Pure Chemical Corporation), and  $\text{TiO}_2$  (Rutile, 99.99 %, Rare Metallic Co., Ltd.) were ground at a molar ratio of 2:1:6 in a glovebox under nitrogen (>99.9995 %) circulation. To obtain a sulfur-rich environment during the reaction, 8 wt% sulfur powder (M 75  $\mu\text{m}$  pass, 99.99 %, High Purity Chemical Laboratory Co., Ltd.) was added to the precursor. Subsequently, a mixture of  $\text{MgCl}_2$  (99.99 %, Sigma-Aldrich Co.) and  $\text{CaCl}_2$  (95.00 %, FUJIFLM Wako Pure Chemical Corporation) at a molar ratio of 0.527:0.473, which served as a flux, was mixed with the YTOS precursor at a weight ratio of 5:1. It should be noted that the flux reagents were dehydrated by calcination at 450 °C for 2 h before the use. The mixture was sealed in an evacuated quartz tube and calcined in a tube furnace. The calcination temperature was increased from room temperature to 773 K at a ramp rate of 5 K  $\text{min}^{-1}$ , then to 1073 K at a ramp rate of 1 K  $\text{min}^{-1}$ , followed by holding at 1073 K for 3 h before thermal quenching in air. After rinsing the product with water, the raw YTOS was recovered by filtration. To remove the residual sulfur species from the surface, the as-prepared powder was annealed in air at 473 K for 1 h, thoroughly rinsed with distilled water, and dried under vacuum. Finally, to remove surface impurities and residual molten salts from the surface, the powder was stirred in a hydrochloric acid solution (18 wt%) for 40 min, filtered, and dried in vacuum at 313 K overnight. The resultant sample is denoted as the YTOS flux. The crystal structure of YTOS was evaluated by X-ray diffraction (XRD; Cu

$K\alpha$  radiation, Miniflex 300, Rigaku Co.; Figure 1). As shown in Figure 1,  $\text{MgTiO}_3$  and  $\text{Y}_2\text{Ti}_2\text{O}_7$  were detected as heterophase by XRD.

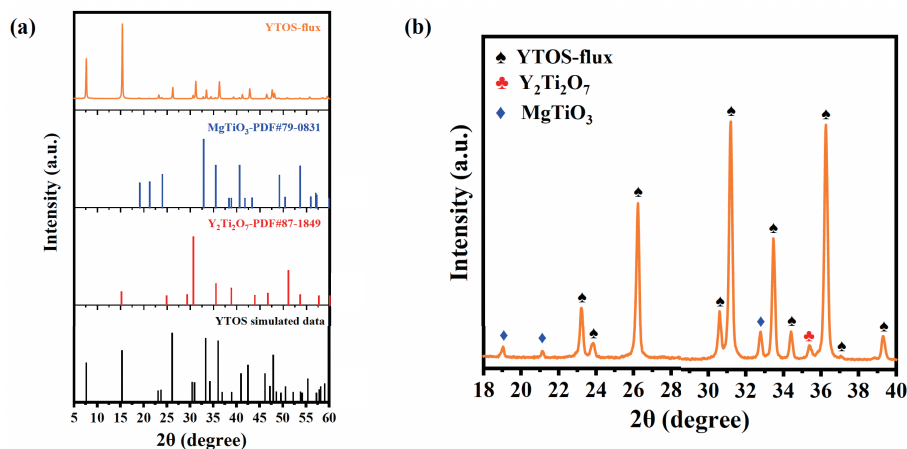


Figure 1: XRD pattern for as-prepared YTOS flux sample (a, orange spectra) and corresponding amplified part (b). The YTOS simulated data refer to the material data by Materials Project.<sup>10</sup>

## TEM observation and atomic resolution STEM-EDS analysis

The YTOS powder was first embedded in G2 resin and sliced using ion milling. The TEM samples were prepared using an ion slicer (EM-09100IS; JEOL). To investigate the local structure inside YTOS, dark-field TEM images and selected area electron diffraction (SAED) patterns were obtained using TEM (JEM-2010HC, JEOL). The weak-beam method was used to observe the dislocations inside the crystal.<sup>11</sup> For higher-resolution observation and composition analysis, atomic-resolution STEM-EDS analysis was conducted using an aberration-corrected STEM (JEM-ARM200F, JEOL) equipped with a silicon drift detector (EDS-SDD, DRY SD, JEOL). The acceleration voltages of TEM and STEM were set to 200 kV.

## Theoretical Investigations

The planar defect in YTOS is investigated using the projector-augmented-wave (PAW) method,<sup>12,13</sup> as implemented in the Vienna ab initio simulation package (VASP),<sup>14–17</sup> within the PBE+ $U$  (Perdew–Burke–Ernzerhof functional<sup>18</sup> with Hubbard  $U$  correction<sup>19</sup>) exchange-correlation functional, with

$U = 7.5$  eV for the  $3d$  orbitals at the Ti sites to reproduce the experimental band gap, 1.9–2.0 eV,<sup>5,20,21</sup> the plane-wave cutoff energy 550 eV, and the Monkhorst-Pack  $15 \times 15 \times 3$   $k$ -point grids in the Brillouin zone. We did not apply a Hubbard  $U$  correction to Y- $4d$  orbitals which does not affect the electronic structure near the band gap, since the Y- $4d$  conduction bands lie in a much higher energy region compared to the Ti- $3d$  levels. Spin-polarized calculations were performed without spin-orbit coupling throughout this work. For PAW potentials, the core orbitals were set as Y:[Ar] $3d^{10}$ , Ti:[Ne], O:[He], S:[Ne], and Mg:[He]; thus, the numbers of valence electrons were 11(Y), 12(Ti), 6 (O and S), and 10 (Mg). During the structural optimization, both the lattice constants and atomic positions are fully relaxed until the residual Hellmann-Feynman forces become less than 0.01 eV/Å.

We calculated the band structures and density of states (DOS) and investigated the formation energy of the  $\text{MgS}_2$  planar defect in a manner similar to that for point defects<sup>22,23</sup> using

$$E_f = E_D - E_P - \mu_{\text{Mg}} - 2\mu_{\text{S}}, \quad (1)$$

where  $E_D$  and  $E_P$  are the total energies of supercells with and without the  $\text{MgS}_2$  planar defect, respectively, and  $\mu_{\text{Mg}}$  and  $\mu_{\text{S}}$  are chemical potentials of reservoirs Mg and S, respectively. The chemical potentials are dependent upon different experimental conditions, such as S-rich, Mg-poor, etc. To evaluate Eq. (1), we investigate the allowable range of  $\mu_i$  ( $i = \text{Y, Ti, O, S, Mg}$ ) in equilibria with possible phases. We first consider the phase equilibrium of YTOS with the reservoir elements,

$$2\mu_{\text{Y}} + 2\mu_{\text{Ti}} + 5\mu_{\text{O}} + 2\mu_{\text{S}} = E_{\text{YTOS}}. \quad (2)$$

Due to the conditions that the competing deposits of  $\text{Y}_2\text{O}_3$ ,  $\text{Y}_2\text{S}_3$ ,  $\text{TiO}_2$ , and  $\text{Y}_2\text{Ti}_2\text{O}_7$  are not

produced,  $\{\mu_i\}$  satisfy the inequalities,

$$\begin{aligned}
2\mu_Y + 3\mu_S &< E_{Y_2S_3}, \\
2\mu_Y + 3\mu_O &< E_{Y_2O_3}, \\
\mu_{Ti} + 2\mu_O &< E_{TiO_2}, \\
2\mu_Y + 2\mu_{Ti} + 7\mu_O &< E_{Y_2Ti_2O_7}.
\end{aligned} \tag{3}$$

We then introduce the *impurity condition*, which results from subequilibrium for the byproduct  $MgTiO_3$ :

$$\mu_{Mg} + \mu_{Ti} + 3\mu_O \approx E_{MgTiO_3}. \tag{4}$$

The total energies of  $Y_2S_3$  (space group:  $P2_1/m$ ),<sup>24</sup>  $Y_2O_3$  ( $Ia\bar{3}$ ),<sup>25</sup> Rutile  $TiO_2$  ( $P4_2/mnm$ ),<sup>26</sup>  $Y_2Ti_2O_7$  ( $Fd\bar{3}m$ ),<sup>27</sup> and  $MgTiO_3$  ( $R\bar{3}$ )<sup>28</sup> are used for  $E_i$ . In addition, we introduce the difference in chemical potential relative to the bulk precipitate,

$$\Delta\mu_i = \mu_i - \mu_{i(bulk)} < 0 \quad (i = Y, Ti, O, S, Mg). \tag{5}$$

The inequality means that bulk precipitates do not decrease. We approximate the bulk chemical potentials by total energies,  $\mu_{i(bulk)} \approx E_{i(bulk)}$ , derived from  $Y(P6_3/mmc)$ ,<sup>29</sup>  $Ti(P6_3/mmc)$ ,<sup>30</sup>  $\alpha$ -S ( $Fddd$ ),<sup>31</sup>  $Mg(P6_3/mmc)$ ,<sup>32</sup> and  $O_2$  molecule (bond length: 1.22 Å).

## Results and Discussion

### TEM and STEM analysis

A bright-field TEM image of a YTOS crystallite is shown in Figure 2a. The SAED pattern (Figure 2a, upper right) obtained from the YTOS crystallite indicates that the synthesized YTOS was a single crystal with good crystallinity. When the dark-field TEM image of the same crystal was acquired using the weak-beam method, a strong bright-line contrast was observed at the center

of the YTOS crystallite (Figure 2b). The bright-line contrast indicates the presence of a planar defect. In order to observe the detailed atomic structure and composition of the planar defect, atomic-resolution STEM observation was performed.

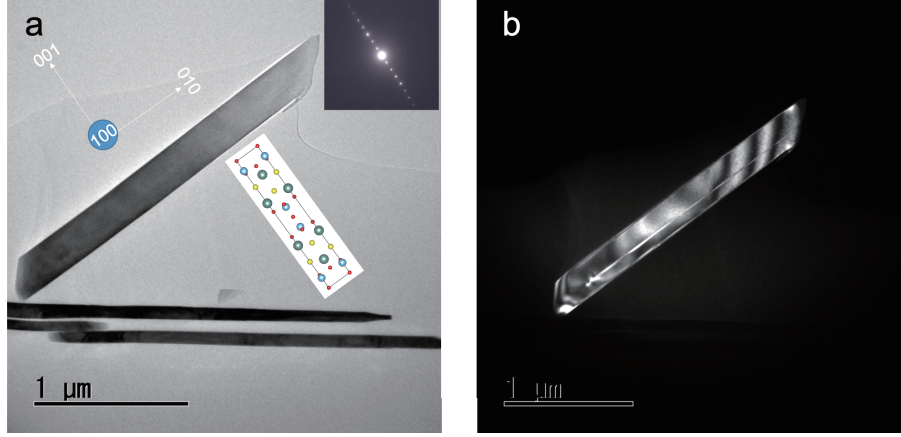


Figure 2: Bright field TEM image (a) and dark-field TEM image taken by the weak-beam method (b) of a YTOS crystallite.

ADF-STEM images (Figure 3a), a straight-line contrast was observed at the same position in the dark-field image of Figure 2. The magnified ADF STEM image of the part surrounded by the square in Figure 3a is shown in Figure 3b. In Figure 3b, the lattice periodicity along  $\langle 001 \rangle$  direction clearly changes in the layers indicated by the arrow.

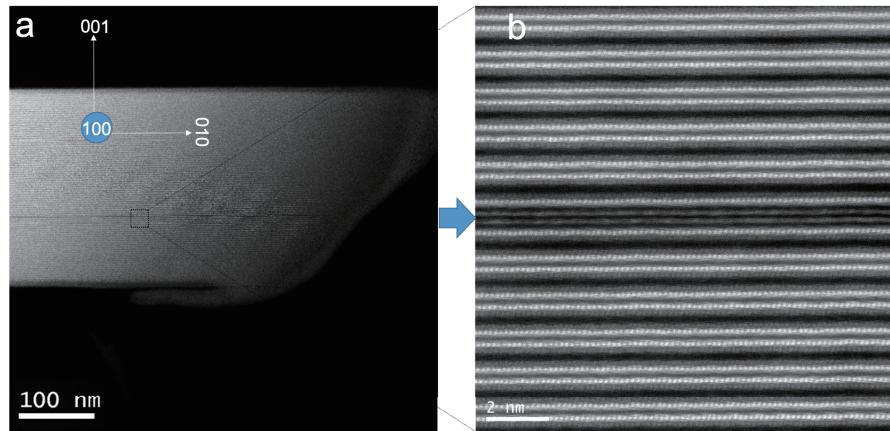


Figure 3: ADF images of a YTOS crystallite.

Figure 4 shows the results of STEM-EDS elemental mapping. It is clear that there are atomic layers with Mg and S segregation in the planar defect. In addition, the Ti, O, and Y signals were

reduced in the same atomic layers. As a result, the defect is considered to be composed of S-Mg-S atomic layers. We investigate this layered structure in detail by first-principles calculations in the following section.

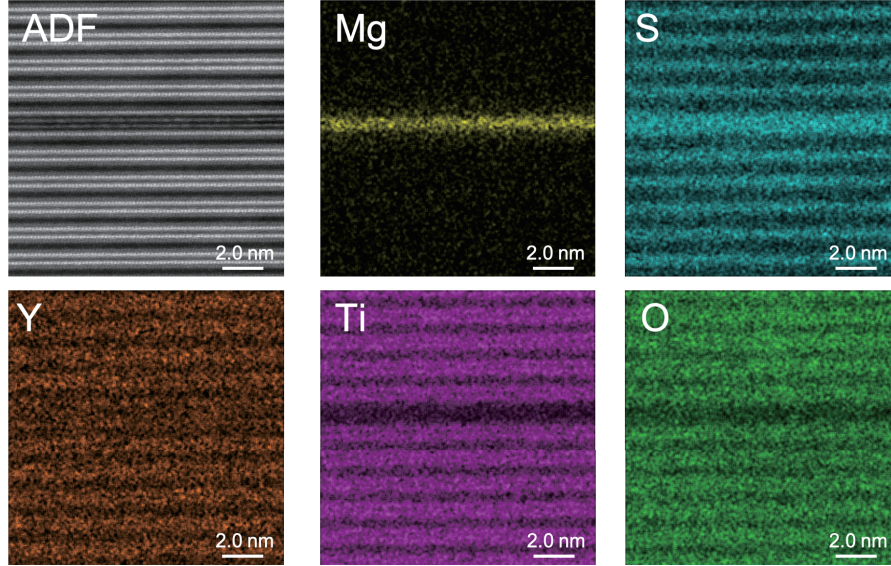


Figure 4: STEM-EDS elemental maps for a planar defect in YTOS crystallite.

## Defect structure

Based on the TEM analysis, we theoretically modeled a plausible structure of the planar defect, as depicted in Figure 5, where a Mg atom is centered in the *ab*-square intersecting the defect S layers. The perfect crystal structure of YTOS is also provided for reference. We also examined the Mg-bridged structure, where the S ligands of Y were bridged by the Mg atom along the *c*-axis, which proved to be less stable. The distance between the Y layers of the defect model, 9.93 Å, is in quantitative agreement with the experimental value, ca. 10.00 Å, from the TEM image. Pure PBE has approximately the same crystal structure, and the non-magnetic configuration is more stable for both PBE and PBE+*U* than the spin-parallel and spin-anti-parallel configurations on the two S atoms neighboring Mg. It was also confirmed that the incommensurate structures in the doubled *ab*-plane using the  $\sqrt{2} \times \sqrt{2} \times 1$  supercell for the Mg-centered structure did not alter the nonmagnetic character, but the optimized structure in the absence of Mg or S in the planar defect

did not reproduce the TEM data.

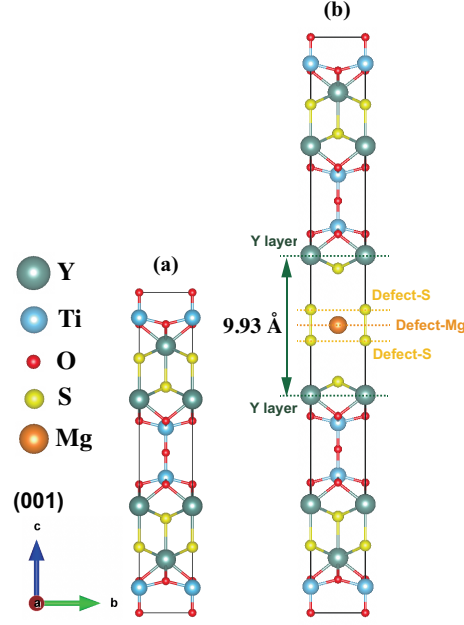


Figure 5: (a) The optimized structure of the conventional unit cell of YTOS, where the atomic positions are relaxed keeping the experimental lattice constants,  $a = b = 3.770 \text{ \AA}$  and  $c = 22.806 \text{ \AA}$ .<sup>33,34</sup> (b) The optimized structures of YTOS supercells with the MgS<sub>2</sub> planar defect in Mg-centered structure. The lattice constants and atomic positions were fully relaxed. These crystal structures were depicted using the VESTA software.<sup>35</sup>

## Electronic structure

The projected DOS (PDOS) of YTOS without a planar defect is shown in Figures 6a and 7a, respectively. The direct band gap of ca. 1.95 eV at the  $\Gamma$  point indicates a nonmagnetic semiconductor. The main characteristics of the valence and conduction bands are S-3*p* and Ti-3*d*, respectively, which is consistent with the results of previous numerical studies.<sup>21,34</sup> We show the PDOS of YTOS with a planar defect in Figure 6b. This defect induces an indirect gap of ca. 0.17 eV, and the valence bands mainly consist of defect levels, namely the S-3*p* bands originating from the planar defect. This agrees with the result of more reliable Heyd-Scuseria-Ernzerhof (HSE06) functional<sup>36</sup> with fixed lattice constants and atomic positions from PBE+*U*, besides the slightly increased band gap, ca. 0.49 eV. The band structure is shown in Figure 7b. The weights of the defect S-3*p<sub>x,y</sub>*, S-3*p<sub>z</sub>*, and Mg-3*s* are indicated by circles, revealing the main characteristics of the

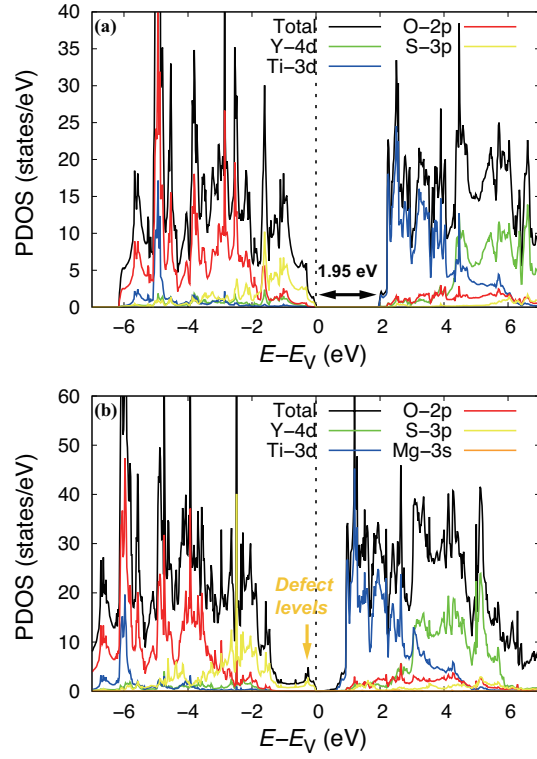


Figure 6: PDOS for YTOS (a) without and (b) with the planar defect. The black line is the total DOS in both cases, while the green, blue, red, and yellow lines denote the PDOS for Y-4d, Ti-3d, O-2p, and S-3p, respectively. The energy ( $E$ ) for each case is measured from the valence band maximum ( $E_V$ ).



valence and conduction bands, defect  $S-3p_{x,y}$  and  $Mg-3s$ , respectively. The large dispersion of the bands reflects the planar (two-dimensional) nature of the defect in S and Mg with a high state density, in contrast to point defects. This is not a numerical artifact owing to the finite size effect of the supercell model. Although the planar defect is naively expected to possess a p-type doping character due to the formal charge of  $MgS_2$  where two electrons are missing from the perfect ions  $Mg^{2+}$  and  $S^{2-}$ , the obtained electronic structure is a narrow-gap semiconductor with a finite gap due to a pair of the defect  $S-3p_z$  levels moving toward the high energy side within the conduction bands. Consequently, the defect bands considerably increase the electron-hole recombination rate, enhancing the interband transitions of the defect valence and/or defect conduction bands via radiative or nonradiative transitions, which is an undesirable factor for the efficiency of the overall water splitting of YTOS.

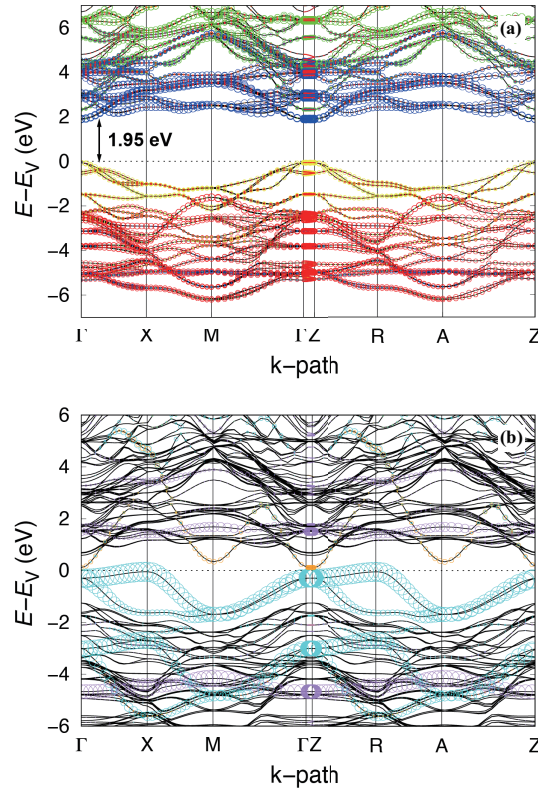


Figure 7: (a) Band structure of YTOS. The orbital weights are indicated by the same colors in Figure 6. (b) Band structure with the planar defect. The defect  $S-3p_{x,y}$ ,  $S-3p_z$ , and  $Mg-3s$  weight are colored in cyan, purple, and orange, respectively.

## Formation energy

The potential range of  $\mu_i$  for the YTOS is obtained by removing  $\mu_O$  in (2) and (3) for a fixed  $\Delta\mu_S$  as the input variables. The phase diagrams as functions of  $\Delta\mu_{Ti}$  and  $\Delta\mu_Y$  are shown for S-rich ( $\Delta\mu_S = 0$  eV) and S-poor ( $\Delta\mu_S = -1.92$  eV) conditions in Figure 8. The YTOS was stable within the area of the ABC triangles. YTOS was synthesized experimentally in an S-rich environment. The sides of the ABC triangle are the phase boundaries of YTOS with the other compounds.  $\Delta\mu_i$  ( $i = Y, Ti, O, S, Mg$ ) at A, B, and C under S-rich and S-poor conditions are listed in Table 1, where  $\Delta\mu_{Mg}$  is obtained from Eq. (2) and (4),  $\Delta\mu_S = -1.92$  eV for S-poor is the minimum required to guarantee  $\Delta\mu_{Ti}$  remains negative within a triangle.

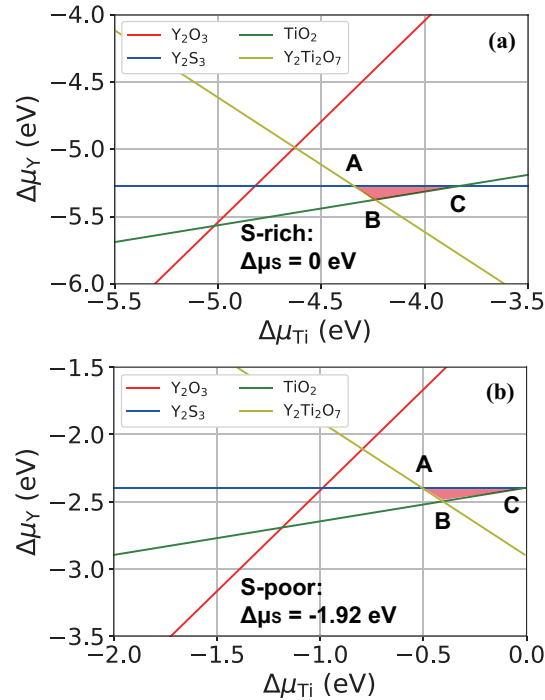


Figure 8: Quaternary phase diagram of YTOS with respect to  $\Delta\mu_{Ti}$  and  $\Delta\mu_Y$  for (a) S-rich and (b) S-poor condition. The phase boundary between YTOS and  $Y_2O_3$ ,  $Y_2S_3$ ,  $TiO_2$ , and  $Y_2Ti_2O_7$  are the red, blue, green, and yellow line, respectively.

Figure 9 shows  $E_f$  as a function of  $\Delta\mu_S$  for points A, B, and C in the phase diagram.  $E_f$  increased with decreasing  $\Delta\mu_S$  and/or  $\Delta\mu_{Mg}$ . Therefore, the optimum conditions for the S and Mg environments must be optimized for the synthesis of YTOS, which suppresses the formation of the planar defect.

**Table 1:**  $\Delta\mu_i$  ( $i = \text{Y, Ti, O, S, Mg}$ ) in eV at points A, B, C in the (Left) S-rich and (Right) S-poor conditions.

S-rich	$\Delta\mu_{\text{Ti}}$	$\Delta\mu_{\text{Y}}$	$\Delta\mu_{\text{O}}$	$\Delta\mu_{\text{Mg}}$	S-poor	$\Delta\mu_{\text{Ti}}$	$\Delta\mu_{\text{Y}}$	$\Delta\mu_{\text{O}}$	$\Delta\mu_{\text{Mg}}$
A	-4.34	-5.27	-2.70	-2.77	A	-0.51	-2.40	-4.62	-0.86
B	-4.24	-5.37	-2.70	-2.87	B	-0.41	-2.50	-4.62	-0.96
C	-3.84	-5.27	-2.90	-2.67	C	-0.00	-2.40	-4.82	-0.75

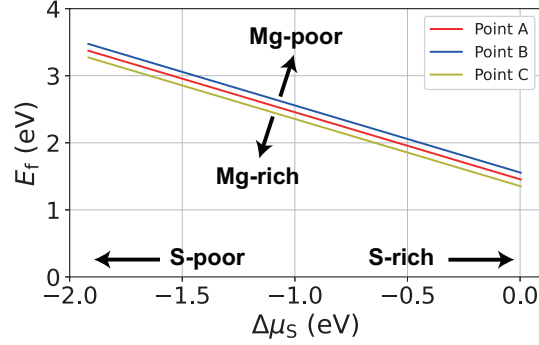


Figure 9: Formation energy of the  $\text{MgS}_2$  planar defect  $E_f$  against  $\Delta\mu_{\text{S}}$ . The red, blue, and yellow lines represent  $E_f$  at points A, B, and C of the phase diagram, respectively.

## Conclusion

In this study, the planar defect structure formed in YTOS crystallites was characterized using (S)TEM and first-principles calculations. It was found that the planar defect is composed of Mg-S-Mg atomic layers by atomic-resolution STEM EDS elemental mapping. First-principles calculations show that although the  $\text{MgS}_2$  planar defect is expected to introduce hole carriers, the obtained electronic structure is a narrow-gap semiconductor with a finite gap, owing to a pair of defect S- $3p_z$  levels moving toward the high-energy side within the conduction bands. Consequently, the defect bands considerably increase the electron-hole recombination rate, enhancing the interband transitions of the defect valence and/or defect conduction bands via radiative or nonradiative transitions, which is an undesirable factor for the overall water splitting efficiency of YTOS. Furthermore, the calculation results of the quaternary phase diagram of YTOS and the formation energy of the  $\text{MgS}_2$  planar defect need to be elaborated for the synthesis of YTOS, which suppresses the formation of the planar defect. It is expected that photocatalysts without defects that can cause recombination will be synthesized in order to achieve efficient solar hydrogen production.

## Acknowledgement

This work was partially supported by the “Advanced Research Infrastructure for Materials and Nano-technology in Japan (ARIM)” of the Ministry of Education, Culture, Sports, Science and Technology (MEXT), Grant Number JPMXP1222UT0023, the Artificial Photosynthesis Project (ARPCChem) of the New Energy and Industrial Technology Development Organization (NEDO), MEXT as “Program for Promoting Researches on the Supercomputer Fugaku” (Realization of innovative light energy conversion materials, Grant Number JPMXP1020210317), and JSPS KAKENHI Grant, 21K04866, 22H00316. All numerical calculations were performed using the supercomputing system at the Institute for Solid State Physics (ISSP) Supercomputer Center of the University of Tokyo and the supercomputer Fugaku provided by RIKEN through the HPCI System Research Project (Project ID: hp210251).

## References

- (1) Kudo, A. Photocatalysis and solar hydrogen production. Pure and Applied Chemistry **2007**, 79, 1917–1927.
- (2) Goto, Y.; Hisatomi, T.; Wang, Q.; Higashi, T.; Ishikiriya, K.; Maeda, T.; Sakata, Y.; Okunaka, S.; Tokudome, H.; Katayama, M. et al. A Particulate Photocatalyst Water-Splitting Panel for Large-Scale Solar Hydrogen Generation. Joule **2018**, 2, 509–520.
- (3) Nishiyama, H.; Yamada, T.; Nakabayashi, M.; Maehara, Y.; Yamaguchi, M.; Kuromiya, Y.; Nagatsuma, Y.; Tokudome, H.; Akiyama, S.; Watanabe, T. et al. Photocatalytic solar hydrogen production from water on a 100-m<sup>2</sup> scale. Nature **2021**, 598, 304–307.
- (4) Takata, T.; Jiang, J.; Sakata, Y.; Nakabayashi, M.; Shibata, N.; Nandal, V.; Seki, K.; Hisatomi, T.; Domen, K. Photocatalytic water splitting with a quantum efficiency of almost unity. Nature **2020**, 581, 411–414.

- (5) Wang, Q.; Nakabayashi, M.; Hisatomi, T.; Sun, S.; Akiyama, S.; Wang, Z.; Pan, Z.; Xiao, X.; Watanabe, T.; Yamada, T. et al. Oxysulfide photocatalyst for visible-light-driven overall water splitting. Nature Materials **2019**, 18, 827–832.
- (6) Pan, Z.; Yoshida, H.; Lin, L.; Xiao, Q.; Nakabayashi, M.; Shibata, N.; Takata, T.; Hisatomi, T.; Domen, K. Synthesis of  $\text{Y}_2\text{Ti}_2\text{O}_5\text{S}_2$  by thermal sulfidation for photocatalytic water oxidation and reduction under visible light irradiation. Research on Chemical Intermediates **2021**, 47, 225–234.
- (7) Ma, G.; Kuang, Y.; Murthy, D. H. K.; Hisatomi, T.; Seo, J.; Chen, S.; Matsuzaki, H.; Suzuki, Y.; Katayama, M.; Minegishi, T. et al. Plate-like  $\text{Sm}_2\text{Ti}_2\text{S}_2\text{O}_5$  Particles Prepared by a Flux-Assisted One-Step Synthesis for the Evolution of  $\text{O}_2$  from Aqueous Solutions by Both Photocatalytic and Photoelectrochemical Reactions. The Journal of Physical Chemistry C **2018**, 122, 13492–13499.
- (8) Ma, G.; Chen, S.; Kuang, Y.; Akiyama, S.; Hisatomi, T.; Nakabayashi, M.; Shibata, N.; Katayama, M.; Minegishi, T.; Domen, K. Visible Light-Driven Z-Scheme Water Splitting Using Oxysulfide  $\text{H}_2$  Evolution Photocatalysts. The Journal of Physical Chemistry Letters **2016**, 7, 3892–3896, PMID: 27626912.
- (9) Zhang, Z.; Tsuchimochi, T.; Ina, T.; Kumabe, Y.; Muto, S.; Ohara, K.; Yamada, H.; Tennen, S. L.; Tachikawa, T. Binary dopant segregation enables hematite-based heterostructures for highly efficient solar  $\text{H}_2\text{O}_2$  synthesis. Nature Communications **2022**, 13, 1499.
- (10) Persson, K. A. Materials Project (Lawrence Berkeley National Lab, 2016); material data on YTOS (SG:139) <https://doi.org/10.17188/1200585>.
- (11) Saka, H. In The Crystal electron microscopy; Doyama, M., Ogawa, K., Kitada, M., Eds.; Uchida Rokakuho, Tokyo, 1997.
- (12) Blöchl, P. E. Projector augmented-wave method. Phys. Rev. B **1994**, 50, 17953–17979.

- (13) Kresse, G.; Joubert, D. From ultrasoft pseudopotentials to the projector augmented-wave method. Phys. Rev. B **1999**, 59, 1758–1775.
- (14) Kresse, G.; Hafner, J. Ab initio molecular dynamics for liquid metals. Phys. Rev. B **1993**, 47, 558–561.
- (15) Kresse, G.; Hafner, J. Ab initio molecular-dynamics simulation of the liquid-metal–amorphous-semiconductor transition in germanium. Phys. Rev. B **1994**, 49, 14251–14269.
- (16) Kresse, G.; Furthmüller, J. Efficiency of ab-initio total energy calculations for metals and semiconductors using a plane-wave basis set. Computational Materials Science **1996**, 6, 15–50.
- (17) Kresse, G.; Furthmüller, J. Efficient iterative schemes for ab initio total-energy calculations using a plane-wave basis set. Phys. Rev. B **1996**, 54, 11169–11186.
- (18) Perdew, J. P.; Burke, K.; Ernzerhof, M. Generalized Gradient Approximation Made Simple. Phys. Rev. Lett. **1996**, 77, 3865–3868.
- (19) Dudarev, S. L.; Botton, G. A.; Savrasov, S. Y.; Humphreys, C. J.; Sutton, A. P. Electron-energy-loss spectra and the structural stability of nickel oxide: An LSDA+U study. Phys. Rev. B **1998**, 57, 1505–1509.
- (20) Boyer-Candalen, C.; Derouet, J.; Porcher, P.; Moëlo, Y.; Meerschaut, A. The Family of  $\text{Ln}_2\text{Ti}_2\text{S}_2\text{O}_5$  Compounds (Ln=Nd, Sm, Gd, Tb, Dy, Ho, Er, and Y): Optical Properties. Journal of Solid State Chemistry **2002**, 165, 228–237.
- (21) Nandal, V.; Shoji, R.; Matsuzaki, H.; Furube, A.; Lin, L.; Hisatomi, T.; Kaneko, M.; Yamashita, K.; Domen, K.; Seki, K. Unveiling charge dynamics of visible light absorbing oxy-sulfide for efficient overall water splitting. Nature Communications **2021**, 12, 7055.
- (22) Zhang, S. B.; Northrup, J. E. Chemical potential dependence of defect formation energies in GaAs: Application to Ga self-diffusion. Phys. Rev. Lett. **1991**, 67, 2339–2342.

- (23) Freysoldt, C.; Grabowski, B.; Hickel, T.; Neugebauer, J.; Kresse, G.; Janotti, A.; Van de Walle, C. G. First-principles calculations for point defects in solids. Rev. Mod. Phys. **2014**, 86, 253–305.
- (24) Schleid, T. Crystal structures of D-Y<sub>2</sub>S<sub>3</sub> and Y<sub>2</sub>OS<sub>2</sub>. European Journal of Solid State and Inorganic Chemistry **1992**, 29, 1015–1028.
- (25) Paton, M. G.; Maslen, E. N. A refinement of the crystal structure of yttria. Acta Crystallographica **1965**, 19, 307–310.
- (26) Mashimo, T.; Bagum, R.; Ogata, Y.; Tokuda, M.; Okube, M.; Sugiyama, K.; Kinemuchi, Y.; Isobe, H.; Yoshiasa, A. Structure of Single-Crystal Rutile (TiO<sub>2</sub>) Prepared by High-Temperature Ultracentrifugation. Crystal Growth & Design **2017**, 17, 1460–1464.
- (27) Farmer, J. M.; Boatner, L. A.; Chakoumakos, B. C.; Du, M.-H.; Lance, M. J.; Rawn, C. J.; Bryan, J. C. Structural and crystal chemical properties of rare-earth titanate pyrochlores. Journal of Alloys and Compounds **2014**, 605, 63–70.
- (28) Culbertson, C. M.; Flak, A. T.; Yatskin, M.; Cheong, P. H.-Y.; Cann, D. P.; Dolgos, M. R. Neutron Total Scattering Studies of Group II Titanates (ATiO<sub>3</sub>, A<sup>2+</sup> = Mg, Ca, Sr, Ba). Scientific Reports **2020**, 10, 3729.
- (29) Spedding, F. H.; Daane, A. H.; Herrmann, K. W. The crystal structures and lattice parameters of high-purity scandium, yttrium and the rare earth metals. Acta Crystallographica **1956**, 9, 559–563.
- (30) Wood, R. M. The Lattice Constants of High Purity Alpha Titanium. Proceedings of the Physical Society **1962**, 80, 783–786.
- (31) Warren, B. E.; Burwell, J. T. The Structure of Rhombic Sulphur. The Journal of Chemical Physics **1935**, 3, 6–8.

- (32) Jette, E. R.; Foote, F. Precision Determination of Lattice Constants. The Journal of Chemical Physics **1935**, 3, 605–616.
- (33) Hyett, G.; Rutt, O. J.; Gál, Z. A.; Denis, S. G.; Hayward, M. A.; Clarke, S. J. Electronically Driven Structural Distortions in Lithium Intercalates of the  $n = 2$  Ruddlesden - Popper-Type Host  $\text{Y}_2\text{Ti}_2\text{O}_5\text{S}_2$ : Synthesis, Structure, and Properties of  $\text{Li}_x\text{Y}_2\text{Ti}_2\text{O}_5\text{S}_2$  ( $0 < x < 2$ ). Journal of the American Chemical Society **2004**, 126, 1980–1991, PMID: 14971931.
- (34) McColl, K.; Corà, F. Fast lithium-ion conductivity in the ‘empty-perovskite’  $n = 2$  Ruddlesden–Popper-type oxysulphide  $\text{Y}_2\text{Ti}_2\text{S}_2\text{O}_5$ . J. Mater. Chem. A **2021**, 9, 7068–7084.
- (35) Momma, K.; Izumi, F. VESTA 3 for three-dimensional visualization of crystal, volumetric and morphology data. Journal of Applied Crystallography **2011**, 44, 1272–1276.
- (36) Krukau, A. V.; Vydrov, O. A.; Izmaylov, A. F.; Scuseria, G. E. Influence of the exchange screening parameter on the performance of screened hybrid functionals. The Journal of Chemical Physics **2006**, 125, 224106.



# TOC graphic

